SPECIAL TOPIC — A 40th Anniversary Celebration: Physics Research and Innovation at Ningbo University

Nonadiabatic vibronic dynamics at a conical intersection with Morse potentials

Jingwen Li(李静雯)[1,†], Qiang Zhang(张强)[1,†], Panpan Zhang(章盼盼)[1], Ajay Jha[2,3,‡], Fulu Zheng(郑福禄)[1,§], and Hong-Guang Duan(段红光)[1,¶]

[1] *Department of Physics, School of Physical Science and Technology, Ningbo University, Ningbo* 315211, *China*
[2] *Rosalind Franklin Institute, Harwell, Oxfordshire OX*11 0*QX, United Kingdom*
[3] *Department of Pharmacology, University of Oxford, Oxford, OX*1 3*QT, United Kingdom*

(Received 27 May 2026; revised manuscript received 6 September 2026; accepted manuscript online 10 September 2026)

Conical intersections (CIs) are primary pathways for ultrafast nonradiative relaxation in photoexcited molecules, yet their spectroscopic signatures often reflect a complex interplay of electronic motion, vibrational dynamics, and environmental dephasing. This challenge becomes particularly significant when the nuclear coordinate driving the relaxation is strongly anharmonic, since harmonic approximations commonly employed in CI models cannot capture the asymmetric level structure and wave-packet evolution associated with realistic bond-stretching motion. Here, we develop a dissipative two-state, two-mode vibronic model that combines an anharmonic Morse tuning coordinate with a harmonic coupling coordinate and a three-level extension for simulating two-dimensional electronic–vibrational (2DEV) spectroscopy. Reduced density-matrix dynamics are propagated using the hierarchy equations of motion, while absorptive 2DEV spectra are calculated within a phase-matching formalism. To isolate the effect of Morse anharmonicity, we further introduce a parameter-matched fully harmonic reference model with the same local frequencies, potential-surface displacements, electronic coupling, bath parameters, temperature, and initial conditions. The resulting potential-energy surfaces generate an asymmetric branching space in which the same nonadiabatic dynamics appear as rapid population transfer in the adiabatic representation and as a more gradual redistribution in the diabatic representation. The calculated dynamics exhibit coherent oscillations with a dominant component near 620 cm^{-1}, while the 2DEV spectra reveal time-dependent redistribution of vibronic intensity during passage through the intersection region. Unequal vibronic peak spacings and evolving center-line slopes emerge as experimentally testable signatures of anharmonic vibronic coupling and changing electronic–vibrational correlation within the present model. These results demonstrate that anharmonic Morse-based models qualitatively alter how CI dynamics appear in 2DEV spectroscopy.

Keywords: two-dimensional electronic–vibrational spectroscopy, conical intersection, Morse potential, hierarchical equations of motion

PACS: 82.53.Kp, 31.50.Gh, 03.65.Yz, 33.20.Wr

DOI: 10.1088/1674-1056/aea538 **CSTR:** 32038.14.CPB.aea538

1. Introduction

Conical intersections have moved from theoretical curiosities to organizing principles of excited-state chemistry. They are the regions where two electronic potential-energy surfaces (PESs) become degenerate and the Born–Oppenheimer separation of electronic and nuclear motion breaks down most dramatically.[1–3] In that regime, electronic excitation can be converted into nuclear motion on femtosecond timescales, making CIs central to photostability, internal conversion, and photochemical selectivity.[4–6] Their influence is now recognized across systems as diverse as nucleobases,[7–9] retinal chromophores,[10–12] carotenoids,[13,14] photosynthetic pigment–protein complexes[13] and functional molecular materials.[15–17] Recent reviews have argued that they play an excited-state role analogous to that of transition states in ground-state reaction dynamics.[4] The modern question is therefore no longer whether CIs matter, but how their local topology, mode selectivity, and environmental dressing become encoded in observables that an experiment can actually measure.

Because of their central role in excited-state relaxation, understanding the quantum dynamics at CIs has become a major theme in modern theoretical and experimental chemistry. Geometric-phase effects near CIs have also been shown to induce symmetry breaking and spatial localization of nuclear wave packets.[18] Ultrafast spectroscopies, including transient absorption,[19] time-resolved photoelectron spectroscopy,[20] and multidimensional techniques,[21–24] have been used to

[†]These authors contributed equally to this work.
[‡]Corresponding author. E-mail: Ajay.Jha@rfi.ac.uk
[§]Corresponding author. E-mail: zhengfulu@nbu.edu.cn
[¶]Corresponding author. E-mail: duanhongguang@nbu.edu.cn

© 2026 Chinese Physical Society and IOP Publishing Ltd. All rights, including for text and data mining, AI training, and similar technologies, are reserved.

CPB Online-Press

study CI-mediated population transfer. Attosecond stimulated x-ray Raman signals have further been proposed to monitor transient electronic coherences during CI passage.[25] Complementary quantum dynamics simulations employing *ab-initio* multiple spawning, trajectory surface hopping,[26,27] or hierarchy equations of motion (HEOM)[28–30] approaches have provided mechanistic insights. In the present work, the Morse potential is introduced to describe anharmonic nuclear motion in the photoexcited nonequilibrium molecular system beyond the local harmonic approximation, rather than to construct realistic molecular PESs. The focus is not to demonstrate again that a CI can induce nonadiabatic transfer, but to reveal how the form of the nuclear potential is mapped onto 2DEV observables, including peak spacings, peak-intensity redistribution, and peak-specific coherences. The question is difficult because no single experimental observable reports only on population transfer. Transient absorption excels at following evolving excited-state manifolds, time-resolved photoelectron spectroscopy is highly sensitive to electronic character, and two-dimensional electronic spectroscopy can separate coherent from incoherent pathways, but each technique projects the dynamics onto only part of the coupled electron-nuclear problem. Recent ultrafast x-ray measurements on pyrazine have made this point especially vividly by showing that CI passage can create electronic dynamics that are subsequently dephased by the surrounding environment on sub-40 fs timescales.[5] In other words, the observable is shaped not only by the crossing itself, but also by how nuclear motion, coherence, and dissipation are braided together while the wave packet traverses the branching space. A compelling theoretical model therefore has to do more than reproduce a transfer time. It has to connect topology, dynamics, and spectroscopy in one language.

Reduced Hamiltonians remain indispensable for that purpose. The minimal two-state, two-mode picture distills the CI into the smallest active subspace that can still represent a branching space: a tuning coordinate that changes the energy gap between states and a coupling coordinate that mixes them. That framework is valuable because it isolates mechanism without drowning it in full-dimensional complexity. Its main weakness, however, is often not the reduced dimensionality but the default use of harmonic potentials.[31,32] Harmonic models are excellent near equilibrium, but they flatten the asymmetry that becomes important as a wave packet moves away from the Franck–Condon region, changes velocity along the reaction coordinate, or samples bond-stretching motion with strongly nonuniform level spacing.[33–35] In realistic molecular systems, however, vibrational potentials are generally anharmonic away from equilibrium, particularly along bond-stretching and other large-amplitude coordinates. This anharmonicity manifests itself in non-equidistant vibrational level spacings and becomes especially relevant after photoexcitation, when nuclear wave packets may explore regions well beyond the local harmonic regime. Thus, accounting for vibrational anharmonicity is important for establishing a more physically realistic description of excited-state nuclear dynamics. Recent theoretical work on internal conversion with Morse potentials has shown that anharmonicity can shift nonradiative rates substantially and can even reverse the error introduced by harmonic approximations depending on displacement and excitation energy.[36] For CIs, that means anharmonicity is not merely a quantitative correction. It can alter how quickly the packet reaches the crossing, how it bifurcates there, and how much coherence survives after the passage. Motivated by these considerations, in the present work, we retain the mechanistic transparency of a reduced-dimensionality model while introducing anharmonicity directly into the tuning coordinate that governs access to the crossing region. The system is formulated as an effective two-state, two-mode vibronic Hamiltonian composed of an anharmonic Morse tuning mode, a harmonic coupling mode linearly coupled through $h_{12} = \gamma Q_c$, and independent Drude–Lorentz environments treated within the HEOM formalism. For spectroscopic calculations, the framework is extended to include the electronic ground state, enabling visible excitation and infrared detection to be described consistently within a unified nonlinear-response treatment. This construction provides a balance between conceptual simplicity and spectroscopic realism. HEOM is particularly well suited to this problem because it captures nonperturbative system–bath interactions and finite bath memory while remaining compatible with multidimensional optical-response calculations.

Two-dimensional electronic–vibrational (2DEV)[37,38] spectroscopy is the natural place to look for that connection. By correlating visible excitation frequency with infrared detection frequency, 2DEV links electronic preparation directly to the vibrational coordinates that respond during relaxation.[39] The power of the method lies in this mixed-frequency character: it can distinguish where the packet was launched electronically from how that packet is distributed vibrationally at a later waiting time. Previous foundational work established that 2DEV is a direct probe of coupled electronic and nuclear motion and that line-shape metrics such as the center-line slope report on cross-correlations between electronic and vibrational frequency fluctuations. Experimental and theoretical studies on carotenoids further demonstrated that 2DEV can follow wave-packet motion through regions influenced by CIs.[40] Yet the specific signatures expected when the active coordinate is explicitly anharmonic remain underdeveloped. That gap is important because 2DEV is sensitive precisely to the quantities most likely to be distorted by anharmonicity: peak spacing, vibronic cross-peak structure, and waiting-time-dependent line shapes.

In this study, we develop a theoretical framework to capture strong anharmonic vibronic dynamics near a CI and con-

CPB Online In-Press

nect them to 2DEV spectroscopic observables. We construct a two-state-two-mode Hamiltonian with an anharmonic Morse tuning mode and a harmonic coupling mode, thereby incorporating tuning-mode anharmonicity absent in harmonic treatments. The interstate vibronic coupling is linear in the coupling coordinate, $h_{12} = \gamma Q_c$, and vanishes at $Q_c = 0$. Using the HEOM formalism, we follow the real-time wave-packet evolution and quantify branching between diabatic surfaces. We also construct a parameter-matched fully harmonic reference model to distinguish the effects of tuning-mode anharmonicity from those of other model parameters. We further extend the model to a three-state scheme including the ground state, enabling simulation of pump–probe preparation and 2DEV signal generation. Within the HEOM formalism, we calculate 2DEV spectra across different waiting times, revealing spectral shifts and cross-peaks diagnostic of anharmonic vibronic coupling. Our results show that anharmonic potentials qualitatively reshape wave-packet bifurcation dynamics compared to harmonic models, leading to altered timescales and coherence decay patterns. Importantly, the calculated 2DEV spectra demonstrate experimentally verifiable signatures of these anharmonic effects, including frequency shifts of cross peaks near the CI and relaxation-induced broadening. By connecting Morse-based Hamiltonians with spectroscopic observables, this work provides a pathway for interpreting 2DEV experiments in strong anharmonic regimes.

2. Model and parameters

To describe the vibronic dynamics near the CI, we consider two excited electronic states coupled to a tuning mode and a coupling mode. The molecular Hamiltonian can be written as

$$\begin{aligned} H_{\mathrm{mol}} &= |g\rangle h_g \langle g| + |e_1\rangle (h_1 + \epsilon_1)\langle e_1| \\ &\quad + |e_2\rangle (h_2 + \epsilon_2)\langle e_2| + (|e_1\rangle h_{12}\langle e_2| + \mathrm{h.c.}). \end{aligned} \tag{1}$$

Here, h_1 and h_2 denote the vibrational Hamiltonians on the two excited diabatic surfaces, where ϵ_1 and ϵ_2 are the site energies of electronic states. The interstate vibronic coupling is taken as $h_{12} = \gamma Q_c$ with $\gamma = 200\ \mathrm{cm}^{-1}$. The coordinates Q_t and Q_c form the two-dimensional branching space near the CI. When this condition is simultaneously satisfied with the diabatic degeneracy condition, $E_{e_1}(Q_t) = E_{e_2}(Q_t)$, the system reaches the single CI point of the present two-dimensional model. In the dimensionless harmonic-oscillator representation used here, the coupling coordinate is written as $Q_c = (a + a^\dagger)/\sqrt{2}$. In the present model, h_g denotes the vibrational Hamiltonian, in which the tuning mode is described by a Morse potential, while the coupling mode is described by a harmonic potential. Thus, we have

$$\begin{aligned} h_g &= \frac{\hbar\omega_t N_t}{2(N_t+1)}\left(b^\dagger b + bb^\dagger\right) \\ &\quad + \frac{\hbar\omega_t}{4(N_t+1)} + \hbar\omega_c\left(a^\dagger a + \frac{1}{2}\right). \end{aligned} \tag{2}$$

The ground-state vibrational Hamiltonian in Eq. (2) can be decomposed into the tuning-mode Morse contribution and the coupling-mode harmonic contribution as

$$h_g = h_{t,g} + h_c, \tag{3}$$

where

$$h_{t,g} = \frac{\hbar\omega_t N_t}{2(N_t+1)}\left(b^\dagger b + bb^\dagger\right) + \frac{\hbar\omega_t}{4(N_t+1)} \tag{4}$$

is the Morse contribution of the tuning mode on the ground-state diabatic surface, and

$$h_c = \hbar\omega_c\left(a^\dagger a + \frac{1}{2}\right) \tag{5}$$

is the harmonic contribution of the coupling mode. Here, $N_t = \sqrt{8D_t\mu_t/(\hbar^2\beta_t^2)} - 1$ is the algebraic parameter of the Morse oscillator with D_t, β_t, and μ_t denoting the dissociation energy, anharmonic parameter and effective mass of the tuning mode, respectively. Moreover, b and $b^\dagger$ denote the annihilation and creation operators of the Morse oscillator, while a and $a^\dagger$ denote those of the harmonic oscillator. The shifted excited-state Morse surfaces are constructed by displacing the ground-state Morse Hamiltonian along the tuning coordinate. Accordingly, for a displacement d_i on the ith excited diabatic surface, the Morse contribution can be written as

$$\begin{aligned} h_{t,i} &= h_{t,g} + \frac{d_i N_t \omega_t}{2(N_t+1)\sqrt{2}} \\ &\quad \times \left(b^\dagger bb - bb^\dagger b^\dagger - bbb^\dagger + b^\dagger b^\dagger b\right). \end{aligned} \tag{6}$$

The excited-state vibrational Hamiltonians h_1 and h_2 are constructed using Eq. (6) with $i = 1$ and 2, respectively, together with the harmonic coupling mode. This displaced form provides the excited-state potential energy surfaces used in the present model. The vibrational Hamiltonians on the two excited diabatic surfaces are then explicitly written as

$$\begin{aligned} h_1 &= h_{t,1} + h_c \\ &= h_{t,g} + \frac{d_1 N_t \omega_t}{2(N_t+1)\sqrt{2}} \\ &\quad \times \left(b^\dagger bb - bb^\dagger b^\dagger - bbb^\dagger + b^\dagger b^\dagger b\right) + h_c, \end{aligned} \tag{7}$$

$$\begin{aligned} h_2 &= h_{t,2} + h_c \\ &= h_{t,g} + \frac{d_2 N_t \omega_t}{2(N_t+1)\sqrt{2}} \\ &\quad \times \left(b^\dagger bb - bb^\dagger b^\dagger - bbb^\dagger + b^\dagger b^\dagger b\right) + h_c, \end{aligned} \tag{8}$$

where h_c is the harmonic contribution of the coupling mode defined above. The detailed basis representation and construction of the Morse–harmonic model Hamiltonian are provided in Section I of the supporting information (SI). Thus, h_1 and h_2 differ from the ground-state vibrational Hamiltonian through

CPB Online First Press

the displacements d_1 and d_2 along the tuning coordinate, while sharing the same harmonic coupling-mode contribution.

To include dissipation, we assume that the two effective modes are coupled to independent harmonic baths. The environmental Hamiltonian can be written as

$$H_{\mathrm{env}} = \sum_{\alpha}\left[\frac{p_\alpha^2}{2m_\alpha}+\frac{m_\alpha\omega_\alpha^2}{2}\left(x_\alpha+\frac{c_\alpha Q_c}{m_\alpha\omega_\alpha^2}\right)^2 + \frac{q_\alpha^2}{2M_\alpha}+\frac{M_\alpha\nu_\alpha^2}{2}\left(y_\alpha+\frac{d_\alpha Q_t}{M_\alpha\nu_\alpha^2}\right)^2\right]. \tag{9}$$

Here, p_α, x_α, m_α, and ω_α denote the momenta, coordinates, masses, and frequencies of the bath oscillators coupled to the coupling mode, while q_α, y_α, M_α, and ν_α denote those coupled to the tuning mode. The corresponding system–bath coupling strengths are given by c_α and d_α, respectively. The baths are characterized by the spectral densities, which have the form

$$J(\omega) = \frac{2\lambda\omega_{\mathrm{cut}}\omega}{\omega^2+\omega_{\mathrm{cut}}^2}, \tag{10}$$

where λ and ω_{cut} denote the reorganization energy and cutoff frequency, respectively. For simplicity, identical Drude–Lorentz spectral densities are assumed for the tuning and coupling baths with $\lambda = 40\ \mathrm{cm}^{-1}$ and $\omega_{\mathrm{cut}} = 200\ \mathrm{cm}^{-1}$.

The population dynamics and the third-order 2DEV responses are propagated using the HEOM method.[28–30] HEOM treats the system–bath coupling and finite bath memory nonperturbatively through a hierarchy of auxiliary density operators. The detailed derivation, including the Feynman–Vernon influence functional, the Drude bath correlation function, the Matsubara expansion, and the hierarchy equations, is provided in Section II of the SI.

For the population dynamics calculation, we use only the two excited states $|e_1\rangle$ and $|e_2\rangle$. For the 2DEV calculations, we use the full three-level model including the ground state $|g\rangle$. The corresponding transition dipole operators are taken as

$$\hat{\mu}_1 = \hat{\mu}_2 = |g\rangle\langle e_2|, \tag{11}$$

and

$$\hat{\mu}_3 = |g\rangle\left(b+b^\dagger+a+a^\dagger\right)\langle g| + |e_1\rangle\left(b+b^\dagger+a+a^\dagger\right)\langle e_1| + |e_2\rangle\left(b+b^\dagger+a+a^\dagger\right)\langle e_2|. \tag{12}$$

Here, $\hat{\mu}_1$, $\hat{\mu}_2$ and $\hat{\mu}_3$ denote the allowed optical transitions associated with the three laser pulses, respectively. In the present 2DEV model, the first two pulses are visible pulses and the third pulse is an infrared probe pulse. The first visible pulse establishes an electronic coherence between $|g\rangle$ and the initially prepared state $|e_2\rangle$, and the second visible pulse converts this coherence into a ground- or excited-state population. During the waiting time T, the system undergoes vibrational evolution and nonadiabatic population transfer from $|e_2\rangle$ to $|e_1\rangle$. Therefore, the first two interactions use the same transition dipole operator. The absence of a $|g\rangle\langle e_1|$ term follows from the selective-initial-excitation assumption of the present model: the visible pump is resonant with the higher-energy bright state $|e_2\rangle$, whereas $|e_1\rangle$ is treated as optically dark or outside the effective pump bandwidth. This is a model assumption rather than a general selection rule. The third transition dipole operator represents the infrared probing process. It does not change the electronic state, but changes the vibrational quantum number within the same electronic manifold. The operators $b+b^\dagger$ and $a+a^\dagger$ correspond to the vibrational transitions of the Morse tuning mode and the harmonic coupling mode, respectively. Thus, the third pulse probes the vibrational response on the electronic state occupied after the waiting-time evolution. The detailed construction of the 2DEV signal and the associated phase-selected response functions are provided in Section III of the SI.

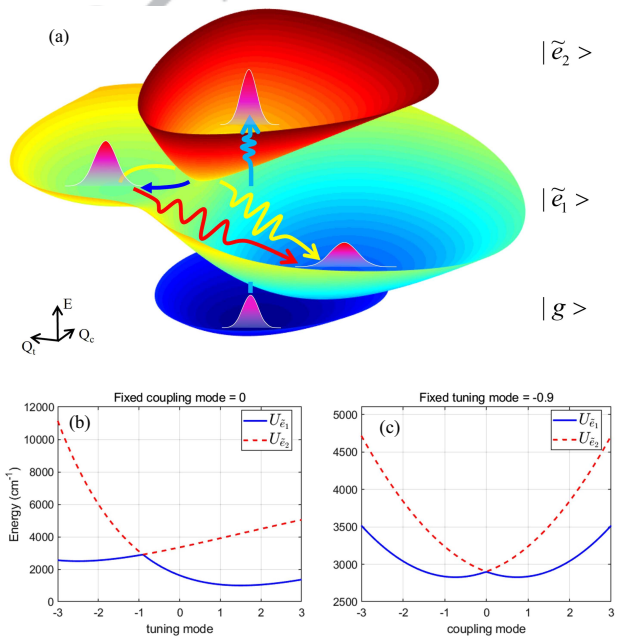


Fig. 1. Anharmonic CI landscape used in the model. (a) Ground ($|g\rangle$) and excited adiabatic potential-energy surfaces ($|\tilde{e}_1\rangle$ and $|\tilde{e}_2\rangle$), together with representative photoexcitation and relaxation pathways. (b) One-dimensional cut along the tuning coordinate, Q_t at fixed coupling coordinate ($Q_c = 0$), highlighting the asymmetric Morse-like anharmonicity of the active relaxation coordinate. (c) One-dimensional cut along the coupling coordinate, Q_c near the crossing region, showing the near-degeneracy that defines the branching space.

For the calculations, we have constructed the model with refined parameters. The system parameters that demonstrate the dynamics of the wave packet passing through the CI are shown in Table 1. With the refined parameters, we have constructed the effective PESs, which are shown in Fig. 1(a). The adiabatic states $|\tilde{e}_1\rangle$ and $|\tilde{e}_2\rangle$ are obtained by diagonalizing the diabatic electronic Hamiltonian in the $\{|e_1\rangle, |e_2\rangle\}$ subspace at each nuclear geometry, where the tilde distinguishes the adiabatic representation from the diabatic basis. The curves of PESs at particular positions (along $Q_c = 0$ and $Q_t = -0.9$) are

CPB Online First Press

also shown in Figs. 1(b) and 1(c), respectively. The anharmonicity is clearly evident in the PES of $|\tilde{e}_1\rangle$ (the blue solid line) in Fig. 1(b).

Table 1. Parameters of the two-state-two-mode Hamiltonian with a Morse tuning mode and a harmonic coupling mode. d_i is the dimensionless quantity representing displacement.

Parameters	Value
Dissociation energy of the Morse tuning potential	6405 cm^{-1}
Numbers of retained basis functions for the tuning and coupling modes	10, 6
Fundamental frequencies of the tuning and coupling modes	$\Omega_t = 420$ cm^{-1}, $\Omega_c = 270$ cm^{-1}
Distance traveled along the tuning mode	$d_1 = 1.5$, $d_2 = -2.5$
First and second excited state	1000 cm^{-1}, 2500 cm^{-1}
Electronic coupling strength	200 cm^{-1}

To isolate the specific effect of tuning-mode anharmonicity, we additionally construct a parameter-matched fully harmonic reference model in which both the tuning and coupling modes are described by harmonic potentials. The electronic energy levels, local vibrational frequencies, potential-surface displacements, interstate electronic coupling, environmental parameters, temperature, and initial conditions are kept identical to those of the Morse–harmonic model; only the Morse tuning potential is replaced by a harmonic potential. The detailed construction and corresponding results are provided in Section IV and Figs. S1–S4 of the SI.

3. Results and discussion

3.1. Population dynamics

Using the model and optimized parameters, we first calculated the population dynamics and examined the wavepacket motion. For this, we constructed the effective Hamiltonian matrix using the annihilation and creation operator formalism for the Morse oscillator and employed HEOM to obtain numerically exact results. We calculated the population dynamics and plotted the resulting data in diabatic and adiabatic bases in Figs. 2(a) and 2(b), respectively. In Fig. 2(a), we observed the population transfer from $|e_2\rangle$ to $|e_1\rangle$ with timescales of 72 fs and 2398 fs, respectively. In addition, the $|e_2\rangle$ population reaches a value of 0.4 after 400 fs. Moreover, we also show the population dynamics in the adiabatic basis, which exhibits clear oscillatory dynamics during the initial 500 fs. Interestingly, we observed that the transfer occurs within a timescale of 109 fs. The diabatic and adiabatic populations in Figs. 2(a) and 2(b) represent different projections of the same nonadiabatic dynamics. Because the adiabatic basis follows the instantaneous electronic eigenstates whereas the diabatic basis tracks the fixed electronic-state character, the corresponding population traces exhibit different temporal profiles and therefore yield different fitted timescales. To examine the coherent dynamics, we also analyzed the residuals. For this, we performed a Fourier transform and plotted the resulting data in Fig. 2(c) and the wavelet-related results in Fig. 2(d). We show that a dominant peak at 620 cm^{-1} and its temporal persistence are clearly visible in Fig. 2(d). Based on the calculations of population, we were able to determine the lifetime of transfer through the CI. The model therefore exhibits clear vibronic coherence.

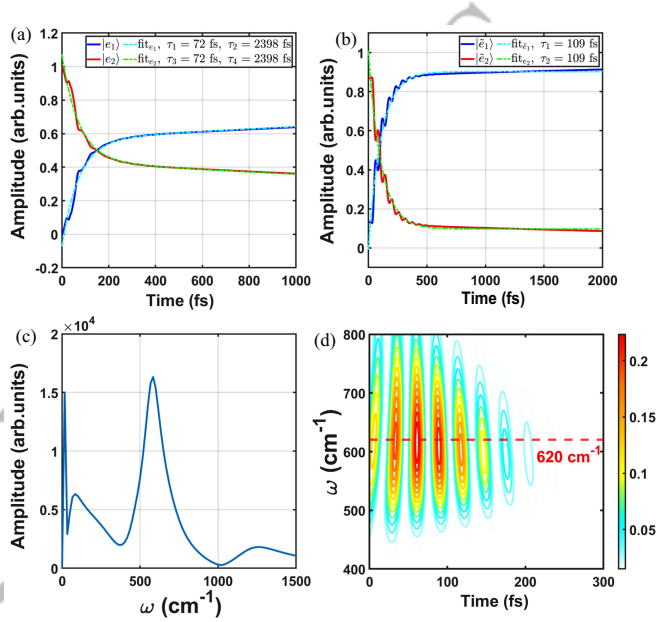


Fig. 2. Population transfer and coherence analysis for the anharmonic CI model. (a) Time-dependent diabatic populations showing a prompt transfer followed by slower redistribution. (b) Adiabatic populations revealing rapid quenching of the upper surface and early-time oscillations associated with coherent passage through the crossing region. (c) Fourier spectrum of the residual dynamics. (d) Wavelet map showing the temporal persistence and decay of the dominant vibrational/vibronic component near 620 cm^{-1}.

3.2. Two-dimensional electronic–vibrational spectra of the CI

After the population dynamics, we also performed the spectroscopic calculations to reveal the anharmonic dynamics near the CI. For this, we employed the phase-matching approach[41,42] with HEOM for the calculations of the 2DEV spectra. The detailed calculations of 2DEV spectra are provided in Section III of the SI. Here, we show the calculated 2DEV spectra with selected waiting times at $T = 0$ fs, 100 fs, 200 fs, 300 fs, 400 fs, and 500 fs, respectively. At $T = 0$ fs, we show the well-separated main and cross peaks (red and blue peaks) in Fig. 3(a). The red (blue) peaks indicate the ground-state-bleaching, GSB or stimulated emission, SE (excited-state absorption, ESA) signals in the 2DEV spectra. We labeled the identified peaks as D, E, F and X, Y, Z, respectively, for clarity. The well-separated red peaks D, E and F are associated with the optical transitions from the ground state $|g\rangle$ to the second excited state $|\tilde{e}_2\rangle$ in the adiabatic basis. The spectroscopic separations between the three peaks are 730 cm^{-1} and 720 cm^{-1}, which correspond to the energy gaps between

CPB Online

two vibrational levels of tuning and coupling modes. The unequal spacings between them demonstrate the anharmonicity of the Morse potential in this model. Interestingly, the blue peaks X, Y, and Z occur at similar excitation frequencies (ω_τ) but at higher energies along the detection axis (ω_t), indicating ESA from higher vibrational levels of $|\tilde{e}_2\rangle$. Based on this, we have demonstrated that the visible excitation and IR probing provide an effective scheme for the detection of nonadiabatic dynamics near the CI.

Figure 3(d) shows the calculated 2DEV spectrum at $T = 100$ fs with similar spectral features, except for the decreased amplitudes of blue peaks X, Y, and Z. This implies that the initial pumped wave packet is moving from higher energy of $|\tilde{e}_2\rangle$ to the lower vibrational levels. At $T = 200$ fs, the labeled peaks D, E, and F show the same spectral features in Fig. 3(b). However, the magnitudes of X, Y, and Z peaks continuously decrease. Moreover, we also observed newly generated blue peaks in Fig. 3(b). We have marked these peaks as A, B, and C, respectively, in Fig. 3(f). These three peaks generally increase in amplitude at $T = 300$ fs (Fig. 3(e)), 400 fs (Fig. 3(c)) and reach a maximum at $T = 500$ fs (Fig. 3(f)). The peaks A, B, and C relate to the ESA of the lower electronic excited state $|\tilde{e}_1\rangle$, which implies that the wave packet has passed through the CI and reached the lower excited state. Thus, we could examine the detailed quantum dynamics near the CI by tracking the time-resolved magnitude of these selected peaks.

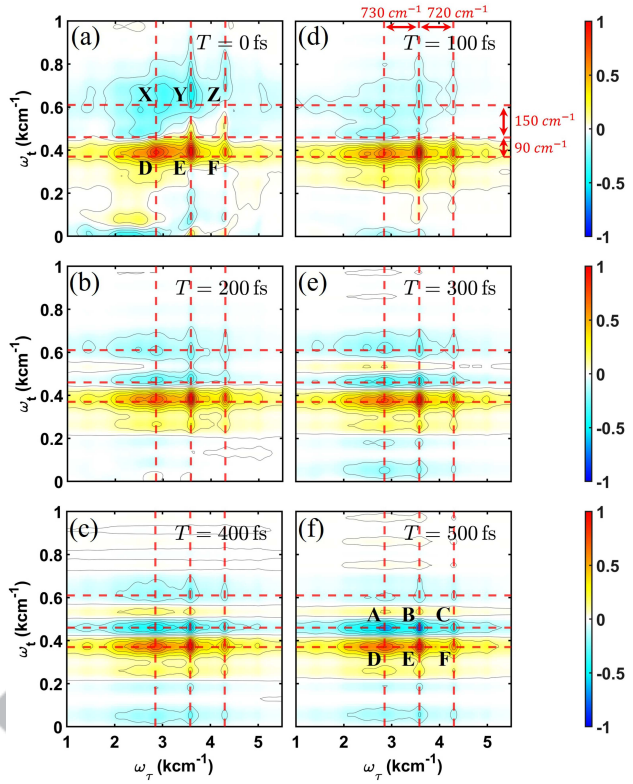


Fig. 3. Waiting-time evolution of the absorptive 2DEV spectra. Early spectra are dominated by positive D/E/F features and negative X/Y/Z features associated with the initially prepared manifold. With increasing waiting time, X/Y/Z decay and A/B/C emerge, providing a direct spectroscopic signature of population transfer to the lower adiabatic surface after passage through the CI. The unequal spacing of the positive peaks reflects the anharmonic vibronic ladder.

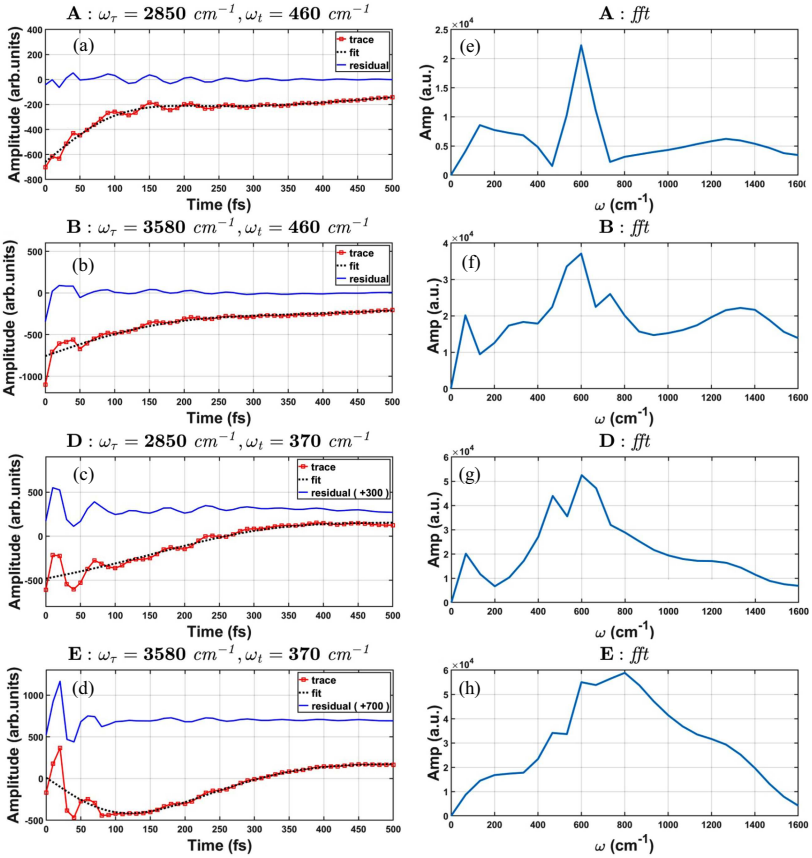


Fig. 4. Peak-selected kinetics and coherence content of the 2DEV response. (a)–(d) Waiting-time traces of representative peaks A, B, D, and E, together with kinetic fits and oscillatory residuals. (e)–(h) Fourier spectra of the residual signals.

3.3. Time-resolved traces and coherent dynamics

In this section, we examined the detailed coherent dynamics revealed from 2DEV spectra. For this, we extracted the magnitudes of the selected peaks as functions of waiting time. We have plotted the time-evolved magnitude of peaks A, B, D, and E as red lines with squares in Figs. 4(a), 4(b), 4(c), and 4(d), respectively. We also fitted the kinetics using exponential functions, shown as black dashed lines. Moreover, we plotted the time-dependent traces as red square markers in Fig. 4 accordingly. We clearly observed the oscillatory dynamics within the initial 400 fs. To examine the coherent dynamics, we performed Fourier transforms and presented the resulting frequency spectra in Figs. 4(e)–4(h). We marked the resolved vibrational modes in the figures. In order to study the coherent dynamics of resolved modes, we have performed wavelet analysis. We show the resulting data in Figs. 5(a)–5(h). We have marked the resolved frequencies as red dashed lines. The details of the wavelet analysis are provided in Section V of the SI. The time-resolved traces, Fourier-transform results, and wavelet analyses of the remaining selected peaks for $\gamma = 200\ \mathrm{cm}^{-1}$ are provided in Section VII and Figs. S5–S7 of the SI.

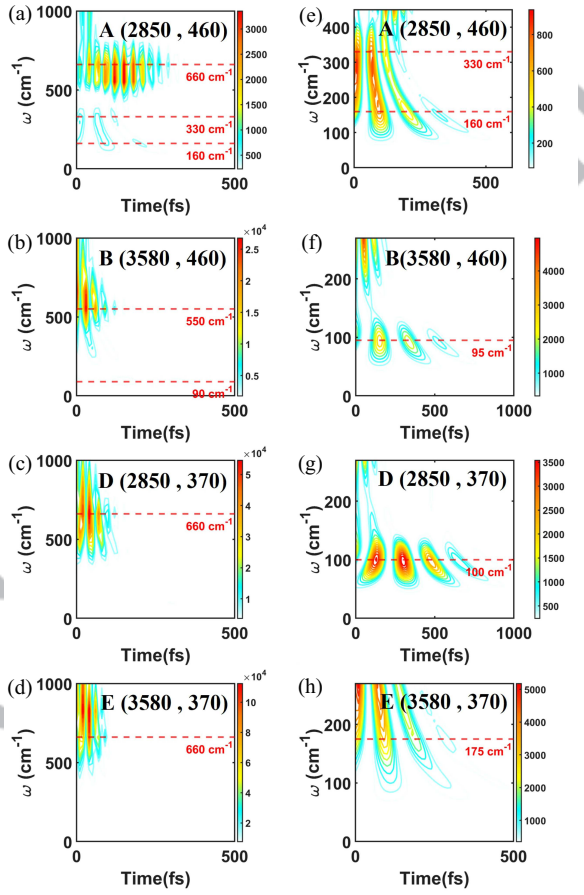


Fig. 5. Wavelet analysis of the selected 2DEV peaks A, B, D, and E. (a)–(d) Wavelet transforms showing the time–frequency structures of the dominant coherent components over the full displayed frequency range. (e)–(h) Corresponding low-frequency regions of the wavelet transforms. For peak A in panel (e), frequencies above 500 cm^{-1} are omitted to highlight the low-frequency coherent components. For peaks B, D, and E in panels (f)–(h), frequencies above 300 cm^{-1} are omitted to emphasize the low-frequency vibrational features.

3.4. Dynamics of center line slope

It has been proposed that the electronic–vibrational dynamics/correlations can be well captured by center line slope (CLS).[38,43,44] The CLS can be defined with respect to either the pump or probe frequency axis: $d_{\mathrm{IR}}/d_{\mathrm{VIS}}$ and $d_{\mathrm{VIS}}/d_{\mathrm{IR}}$. Positive, negative, and zero CLS values indicate positive correlation, negative correlation, and no correlation, respectively. The decay of the CLS reports the loss of electronic–vibrational frequency correlation arising from the combined effects of vibrational evolution, population redistribution, and environmental dephasing. The magnitude of CLS can also be used to estimate the relative coupling strength of the vibrations of two electronic states with the baths.[43,45] The detailed procedure for extracting the local peak centers, constructing the center lines, and determining the CLS lifetimes is provided in Section VI of the SI. The CLS lifetimes of all selected peaks for different interstate coupling strengths are summarized in Table 1 of the SI. Here, we calculated the CLS values for the selected positive and negative peaks using $d_{\mathrm{IR}}/d_{\mathrm{VIS}}$. The dynamics of CLS over time is shown in Fig. 6. The curves in Fig. 6 were fitted using single-exponential functions. We observed that the electronic DoFs are negatively correlated with the tuning mode at the beginning. That is, higher electronic excitation is correlated with lower vibrational frequencies.[45] Here, we focus on the characteristic relaxation/correlation timescale associated with passage through the CI region, a fast non-adiabatic process, and thus use a single exponential fit to distinguish the energy transfer process. The lifetimes of peaks A, B, D, and E are 61 fs, 315 fs, 52 fs, and 142 fs, respectively. The energy difference between the two excited states is 1500 cm^{-1}, so relaxation of the first excited state involves substantial energetic reorganization, as shown by the decay of CLS, which destroys the electron–vibration correlation. In addition, CLS does not reach 0, but it shows a long deviation from 0, which has previously been attributed to a small static inhomogeneous-broadening component.[40] These results also provide insight into the anti-correlation of electronic and vibrational DoFs. Additional

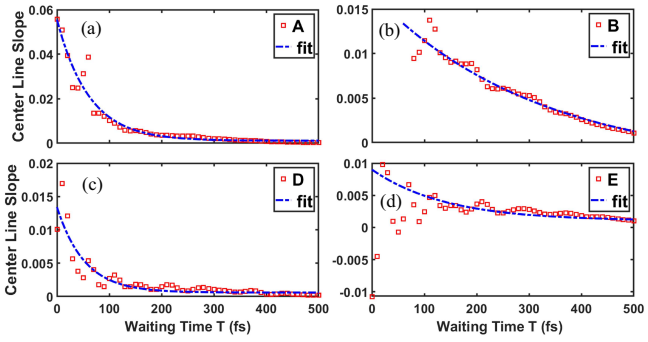


Fig. 6. Center-line-slope dynamics of representative 2DEV peaks A, B, D, and E. The CLS decays report the loss of electronic–vibrational frequency correlation during relaxation and reveal that different spectral windows dephase on different timescales.

2DEV, population-dynamics, coherent-dynamics, and CLS results for $\gamma = 150$ cm^{-1} and 300 cm^{-1} are provided in Sections VIII and IX of the SI, respectively.

4. Discussion

The core finding of the present study is that anharmonicity modifies the spectroscopic manifestation of conical-intersection dynamics in a way that cannot be reduced to a simple change in transfer rate. In the harmonic limit, vibronic progressions and recurrence patterns are often expected to reflect relatively regular energy-level spacing and nearly symmetric motion in the branching space. This contrast is also evident from the parameter-matched fully harmonic reference calculations in Section IV and Figs. S1–S4 of the SI. Relative to the harmonic reference, the Morse–harmonic model exhibits a pronounced slow component in the diabatic population redistribution, a shift of the dominant coherent component from approximately 470 cm^{-1} to 620 cm^{-1}, and a broader distribution of 2DEV spectral features. In the present model, however, the Morse-like tuning coordinate introduces an intrinsically asymmetric structure into the vibronic manifold. This asymmetry appears directly in the 2DEV response through unequal peak separations, nonuniform redistribution of spectral weight, and distinct temporal evolution of the X/Y/Z and A/B/C peak families. The calculations therefore suggest that the anharmonic coordinate participates in determining which vibronic transitions remain spectroscopically active during different stages of the passage through the intersection region. The resulting dynamics are not solely governed by population flow between diabatic surfaces, but also by time-dependent reorganization of the vibrational ladder itself. In this sense, the spectra indicate that anharmonicity reshapes the observable vibronic connectivity associated with the intersection. This interpretation is consistent with broader theoretical work showing that harmonic approximations can become unreliable when the active nuclear coordinate samples regions far from the local quadratic regime or undergoes substantial displacement during nonadiabatic relaxation.

A second outcome concerns the role of 2DEV spectroscopy as a probe of dissipative nonadiabatic dynamics. The present HEOM-based calculations extend earlier studies of open-system conical-intersection dynamics by placing the 2DEV signal, rather than population dynamics alone, at the center of the analysis. Within this framework, the calculations indicate that several components of the intersection dynamics remain experimentally distinguishable even in the simultaneous presence of bath-induced dephasing and anharmonic nuclear motion. In particular, the waiting-time evolution separates signatures associated with intrastate vibrational redistribution from those associated with intersurface transfer. The center-line-slope analysis further shows that the spectral line shape retains information about correlated electronic–vibrational motion beyond simple homogeneous broadening. The persistence and decay of these correlations track changes in the local vibronic environment during relaxation through the intersection region. Although the present model is intentionally reduced, these observations place the calculations in direct conceptual connection with recent experimental efforts aimed at resolving vibronic coherence and ultrafast electronic relaxation in strongly coupled molecular systems using multidimensional optical and x-ray spectroscopies.

At the same time, the simplified structure of the model makes clear the limitations that should be addressed in future work. The present treatment isolates the essential branching-space coordinates in order to establish a transparent connection between conical-intersection topology and spectroscopic response. Extending the approach toward quantitatively realistic systems will require more detailed parameterization of the potential-energy surfaces, inclusion of additional vibrational modes outside the reduced branching space, and treatment of coordinate-dependent transition dipoles and non-Condon effects. Incorporating these ingredients will be important for assessing how robust the present spectral signatures remain in higher-dimensional environments and under stronger solvent coupling. Such developments appear timely given the rapid experimental progress in multidimensional vibrational–electronic spectroscopy, FSRS, and ultrafast x-ray techniques, together with ongoing advances in open-system and nonadiabatic simulation methods. Within this broader context, the present calculations are best viewed not as a replacement for full-dimensional treatments, but as a controlled framework for identifying which spectroscopic signatures arise directly from the interplay of anharmonicity, dissipation, and conical-intersection topology.

5. Conclusion

We have shown that a reduced conical-intersection model becomes substantially more informative when the active tuning coordinate is treated anharmonically and the observables are formulated in the mixed electronic–vibrational domain. Within the present framework, the potential-energy surfaces generate an asymmetric trajectory through the branching space, while the same nonadiabatic evolution appears as rapid depletion of the upper state in the adiabatic representation and as multiscale population redistribution in the diabatic representation. The 2DEV response translates these coupled electronic and nuclear processes into experimentally accessible spectral signatures through the redistribution of peak intensities and the evolution of vibronic correlations. In particular, the unequal vibronic peak spacings, the staged transfer of negative spectral weight from X/Y/Z to A/B/C, the persistence of oscillatory components in the 550–660 cm^{-1} re-

CPB Online In Press

gion, and the peak-specific center-line-slope decay together support a consistent picture of dissipative anharmonic nonadiabatic relaxation near the intersection region. More generally, the present results indicate that the spectroscopic signatures of conical-intersection dynamics depend sensitively on the local structure of the nuclear potential and cannot always be captured within harmonic representations of the branching space. The calculations further demonstrate that 2DEV spectroscopy can distinguish features associated with vibrational redistribution, electronic relaxation, and evolving vibronic correlations even in the presence of environmental dissipation. In this sense, the work establishes a direct connection between conical-intersection topology, anharmonic nuclear motion, and experimentally observable 2DEV spectral response, providing a physically transparent framework for interpreting ultrafast nonadiabatic dynamics in complex molecular systems.

Acknowledgements

This work was supported by the National Key Research and Development Program of China (Grant No. 2024YFA1409800), the National Natural Science Foundation of China (Grant Nos. 12274247, W2421021N, and 12504279), Zhejiang Provincial Natural Science Foundation of China (Grant No. LQN26A040009), Yongjiang Talents Program (Grant Nos. 2022A-094-G and 2023A-158-G), and Ningbo International Science and Technology Cooperation (Grant No. 2023H009).

References

[1] Domcke W, Yarkony D R and Köppel H (eds) 2011 *Conical Intersections: Theory, Computation and Experiment* (Singapore: World Scientific)
[2] Domcke W and Yarkony D R 2012 *Annu. Rev. Phys. Chem.* **63** 325
[3] Schuurman M S and Stolow A 2018 *Annu. Rev. Phys. Chem.* **69** 427
[4] Boeije Y and Olivucci M 2023 *Chem. Soc. Rev.* **52** 2643
[5] Chang Y P, Balciunas T, Yin Z, Sapunar M, Tenorio B N C, Paul A C, Tsuru S, Koch H, Wolf J P, Coriani S and Wörner H J 2025 *Nat. Phys.* **21** 137
[6] Wu Y, Cao J, Ma H, Zhang C, Bian W, Nunez-Reyes D and Hickson K M 2019 *Sci. Adv.* **5** eaaw0446
[7] Lan Z, Frutos L M, Sobolewski A L and Domcke W 2008 *Proc. Natl Acad. Sci. USA* **105** 12707
[8] Cuéllar-Zuquin J, Pepino A J, Fdez Galván I, Rivalta I, Aquilante F, Garavelli M, Lindh R and Segarra-Martí J 2023 *J. Chem. Theory Comput.* **19** 8258
[9] Cerullo G and Garavelli M 2020 *Proc. Natl Acad. Sci. USA* **117** 26553
[10] Kukura P, McCamant D W, Yoon S, Wandschneider D B and Mathies R A 2005 *Science* **310** 1006
[11] Johnson P J M, Halpin A, Morizumi T, Prokhorenko V I, Ernst O P and Miller R J D 2015 *Nat. Chem.* **7** 980
[12] Polli D, Altoè P, Weingart O, Spillane K M, Manzoni C, Brida D, Tomasello G, Orlandi G, Kukura P, Mathies R A, Garavelli M and Cerullo G 2010 *Nature* **467** 440
[13] Liu N, Zhang Y, Niu K, Lu F and Zhong D 2023 *J. Phys. Chem. Lett.* **14** 9215
[14] Polli D, Antognazza M R, Brida D, Lanzani G, Cerullo G and De Silvestri S 2008 *Chem. Phys.* **350** 45
[15] Duan H G, Jha A, Li X, Tiwari V, Ye H, Nayak P K, Zhu X L, Li Z, Martinez T J, Thorwart M and Miller R J D 2020 *Sci. Adv.* **6** eabb0052
[16] Jha A, Duan H G, Tiwari V, Thorwart M and Miller R J D 2018 *Chem. Sci.* **9** 4468
[17] Cui B, Jha A and Duan H G 2024 *J. Phys. B: At. Mol. Opt. Phys.* **57** 105101
[18] Ryabinkin I G and Izmaylov A F 2013 *Phys. Rev. Lett.* **111** 220406
[19] Ruckebusch C, Sliwa M, Pernot P, de Juan A and Tauler R 2012 *J. Photochem. Photobiol. C* **13** 1
[20] Schuurman M S and Blanchet V 2022 *Phys. Chem. Chem. Phys.* **24** 20012
[21] Fresch E, Camargo F V A, Shen Q, Bellora C C, Pullerits T, Engel G S, Cerullo G and Collini E 2023 *Nat. Rev. Methods Primers* **3** 84
[22] Timmer D, Gittinger M, Quenzel T, Cadore A R, Rosa B L T, Li W, Soavi G, Lünemann D C, Stephan S, Silies M, Schulz T, Steinhoff A, Jahnke F, Cerullo G, Ferrari A C, De Sio A and Lienau C 2024 *Nano Lett.* **24** 8117
[23] Biswas S, Kim J, Zhang X and Scholes G D 2022 *Chem. Rev.* **122** 4257
[24] Jha A, Zheng F, Liu Z, Mukamel S, Thorwart M, Miller R J D and Duan H G 2026 *Chem. Soc. Rev.* **55** 1089
[25] Kowalewski M, Bennett K, Dorfman K E and Mukamel S 2015 *Phys. Rev. Lett.* **115** 193003
[26] Merritt I C D, Jacquemin D and Vacher M 2023 *J. Chem. Theory Comput.* **19** 1827
[27] Richardson J O, Lawrence J E and Mannouch J R 2025 *Annu. Rev. Phys. Chem.* **76** 663
[28] Tanimura Y 2020 *J. Chem. Phys.* **153** 020901
[29] Tanaka M and Tanimura Y 2009 *J. Phys. Soc. Jpn.* **78** 073802
[30] Ishizaki A and Tanimura Y 2005 *J. Phys. Soc. Jpn.* **74** 3131
[31] González-Luque R, Garavelli M, Bernardi F, Merchán M, Robb M A and Olivucci M 2000 *Proc. Natl Acad. Sci. USA* **97** 9379
[32] Duan H G, Nalbach P, Prokhorenko V I, Mukamel S and Thorwart M 2015 *New J. Phys.* **17** 072002
[33] Setty C, Baggioli M and Zaccone A 2024 *J. Phys.: Condens. Matter* **36** 173002
[34] Zhao W, Sun Y, Li J, Yuan P, Iitaka T, Zhong X, Li H, Fang Y W, Liu H, Errea I and Xie Y 2025 *npj Comput. Mater.* **11** 347
[35] Zacharias M, Scheffler M and Carbogno C 2020 *Phys. Rev. B* **102** 045126
[36] Wang Y, Ren J and Shuai Z 2021 *J. Chem. Phys.* **154** 214109
[37] Oliver T A A, Lewis N H C and Fleming G R 2014 *Proc. Natl Acad. Sci. USA* **111** 10061
[38] Arsenault E A, Bhattacharyya P, Yoneda Y and Fleming G R 2021 *J. Chem. Phys.* **155** 020901
[39] Zhang X, Liu Z, Jha A, Liang X T, Thorwart M, Miller R J D and Duan H G 2023 *J. Phys. B: At. Mol. Opt. Phys.* **56** 145001
[40] Oliver T A A and Fleming G R 2015 *J. Phys. Chem. B* **119** 11428
[41] Gelin M F, Egorova D and Domcke W 2005 *J. Chem. Phys.* **123** 164112
[42] Gelin M F, Egorova D and Domcke W 2005 *Chem. Phys.* **312** 135
[43] Lewis N H C, Dong H, Oliver T A A and Fleming G R 2015 *J. Chem. Phys.* **142** 174202
[44] Cho M and Fleming G R 2020 *J. Phys. Chem. B* **124** 11222
[45] Dong H, Lewis N H C, Oliver T A A and Fleming G R 2015 *J. Chem. Phys.* **142** 174201

CPB Online IOP Press